



Effect of temperature on the programmable helical deformation of a reconfigurable anisotropic soft actuator

Dong Wang^{a,b,*}, Ling Li^a, Biao Zhang^{b,c}, Yuan-Fang Zhang^b, Mao See Wu^d, Guoying Gu^{a,*}, Qi Ge^{b,e,*}

^a Robotics Institute and State Key Laboratory of Mechanical System and Vibration, School of Mechanical Engineering, Shanghai Jiao Tong University, Shanghai 200240, China

^b Digital Manufacturing and Design Centre, Singapore University of Technology and Design, Singapore 487372, Singapore

^c Xi'an Institute of Flexible Electronics and Xi'an Key Laboratory of Biomedical Materials & Engineering, Northwestern Polytechnical University, Xi'an 710072, Shaanxi, China

^d School of Mechanical and Aerospace Engineering, Nanyang Technological University, 50 Nanyang Avenue, Singapore 639798, Singapore

^e Department of Mechanical and Energy Engineering, Southern University of Science and Technology, Shenzhen 518055, China

ARTICLE INFO

Article history:

Received 6 September 2019

Revised 7 April 2020

Accepted 20 April 2020

Available online 18 May 2020

Keywords:

Reconfigurable soft actuator

Thermal response

Helical deformation

Multi-material 3D printing

ABSTRACT

Shape reconfiguration is ubiquitous in nature and widely used in many applications such as soft robotics, metamaterials, energy absorption and tissue engineering. Shape reconfigurable soft actuators, due to their ability to adapt and adjust in complex and unpredictable working environment, have been designed by the use of various delicate structures and active materials. However, soft actuators that exhibit reconfigurable helical deformation have not been proposed; they have the advantage of integrating both bending and twisting actuations in one deformation mode. In this work, we present a thermal-induced shape reconfigurable soft actuator that shows reversible actuations with vastly shape differences under thermal stimulus. It exhibits helical deformation at lower temperature and mainly in-plane bending at relatively higher temperature. The reversible shape transition is controlled by a thermal stimulus that changes the anisotropy of the structure, which consists of shape memory polymer fibers embedded in a homogeneous elastic matrix. A theoretical model is proposed based on the minimum potential energy that incorporates the thermomechanical behavior of the shape memory polymer fibers. Experiments are conducted and the results agree well with the theoretical modeling. Using the theoretical model, we establish design principles for reconfigurable soft actuators whose functional response is programmable given the architecture and external stimulus. A six-handed helical soft actuator, constructed to demonstrate its programmable deformation, is utilized to catch a living fish in water.

© 2020 Elsevier Ltd. All rights reserved.

1. Introduction

Shape reconfiguration, or the shape transition between multiple morphologies under external stimuli, is ubiquitous in nature. For example, Venus flytrap catches its prey by a transition of its leaves from open to close when the tiny hair on the inner surfaces is triggered by insects (Forterre et al., 2005). The scales of pine cone change from close to open to release its seeds when stimulated by the changes in relative humidity (Dawson et al., 1997). Shape reconfiguration has also attracted considerable attentions in various applications, such as soft robotics (Cestari et al., 2014; Gu et al.,

2018; Wang et al., 2018b, 2018c; Zhang et al., 2019), high performance metamaterials (Bertoldi et al., 2017), energy absorption (Janke et al., 2005), aerospace (Sofla et al., 2010) and tissue engineering (Zhao et al., 2018).

Reconfigurable soft actuators, which can significantly modulate their mechanical response to environment by their flexibility and adaptability, have been actively studied recently. Various materials have been employed to realize the shape reconfiguration, such as shape memory polymer (SMP), shape memory alloy (SMA), granular particles, magnetorheological fluid etc. Among these, SMP has the advantage of high ratio between the maximal and the minimal rigidity, which facilitates its use in shape reconfigurable soft actuators. For example, Tobushi et al. developed a thermal tunable soft actuator by using SMP that could exhibit multiple bending actuation modes (Tobushi et al., 2006). Ghosh et al. designed a multi-

* Corresponding author.

E-mail addresses: wang_dong@sjtu.edu.cn (D. Wang), guguoying@sjtu.edu.cn (G. Gu), geq@sustech.edu.cn (Q. Ge).

state SMP composite that can perform different functions at different states (Ghosh et al., 2013). Takashima et al. designed a bending pneumatic artificial muscle whose bending curvature can be controlled by the heating of an SMP sheet (Takashima et al., 2014).

However, most of the shape reconfigurable soft actuators proposed previously only allow bending as the main motion and are thus far from approaching the level of complexity of biological architectures. Helical actuation, as a combination of both bending and twisting, has the advantage of two actuation modes operating simultaneously and has been widely adopted in nature and engineering, such as the elephant trunks for grasping (Hannan and Walker, 2003), plant tendril for climbing (Gerbode et al., 2012) and bacterial flagella for locomotion (Mendelson, 1978). Despite the promising application of shape reconfigurable helical soft actuator, its development with tunable behaviors has been hindered due to the lack of efficient fabrication tools and modeling approaches. Fabrication of helical soft actuators is limited as they are mainly made of a single material, making them difficult to generate anisotropy which results in helical motion. The lack of theoretical modeling framework also restricts the design and programming of the reconfigurable soft actuators. Several models for soft actuators have been proposed recently (Connolly et al., 2017; de Payrebrune and O'Reilly, 2016; Gorissen et al., 2013; Hao et al., 2017; Matia and Gat, 2015; Polygerinos et al., 2015). For example, analytical model based on nonlinear elasticity is developed to model the bending, extension, expansion and twist motions of a fluid-powered fiber-reinforced actuator (Connolly et al., 2017). A rod-based model is proposed to model the bending behavior of a constraint pneu-net actuator (de Payrebrune and O'Reilly, 2016). However, the helical deformation is not considered. An anisotropic soft actuator is fabricated by embedding aligning fibers into an elastomer matrix and its helical actuation is predicted by a theoretical framework (Wang et al., 2018a). This soft actuator, however, exhibits only one shape under actuation.

In this work, we propose a 3D printed shape reconfigurable anisotropic soft actuator (SRASA) that is capable to changes its anisotropy and thus shows vastly different configurations under thermal stimulus. The anisotropy is generated by 3D printing aligned SMP fibers inside an elastomeric matrix. Under a thermal stimulus, the elastic modulus of the SMP fibers vary from the order of MPa to GPa and thus the anisotropy of the structure changes significantly. In order to capture the reconfigurable deformations, a theoretical framework based on the minimum potential energy method that takes into account the thermomechanical behaviors of the SMP fibers is proposed and verified by experiments. The new contribution consists of the study of the dependence of the helical configuration on the thermal stimulus, and the experimental verification of the predicted shape change with temperature.

Following this introduction, we presented the geometrical design, theoretical modeling, experimental validation, numerical results, a biomimetic designed gripper and conclusions in six sections.

2. Geometrical design of the SRASAs

The SRASA is designed by Solidworks (3DS Dassault Systemes, France) as shown in Fig. 1. It is a rectangle block with length L , width W and height H . It consists of two layers: a fiber reinforced top layer with thickness h_1 and a bottom layer of matrix materials with thickness h_2 . The fiber is oriented at an angle ϕ_0 from the length direction. A small channel with square cross-section all through the length direction at a distance h_c below the top surface is designed for embedding a control cable. One end of the control cable and one end of the actuator are firmly bonded and the cable is able to move inside the channel with negligible friction. By

pulling the end of the cable with a displacement Δd , a compressive force F is generated and the SRASA deforms.

3. Theoretical modeling

In this section, the reconfigurable deformation of SRASA is modeled. We first use a thermomechanical multi-branch model to characterize the dependence of the mechanical behaviors of the fiber materials on ambient temperature. The relation of Young's modulus and temperature is then incorporated into a theoretical model based on minimum potential energy method to model the reconfigurable deformation of the SRASAs.

3.1. Thermomechanical behavior of the fiber

In order to characterize the dependence of the fiber's elastic modulus on temperature, a thermomechanical multi-branch model is adopted to model fiber (Ge et al., 2014; Westbrook et al., 2011; Yu et al., 2014a). The model consists of one equilibrium branch associated with the elastic response and several non-equilibrium branches (number of n) associated with viscoelastic response. Each non-equilibrium branch is taken to be a Maxwell element. For a 1D multi-branch model, the temperature dependent storage modulus $E_f(T)$, and $\tan \delta(T)$ of the SMP fiber can be expressed as (Yu et al., 2014a, 2014b):

$$E_f(T) = E_{eq} + \sum_{i=1}^n \frac{E_i w^2 \tau_i(T)^2}{1 + w^2 \tau_i(T)^2}, \quad (1)$$

$$\tan \delta(T) = \frac{E_l(T)}{E_f(T)}. \quad (2)$$

where E_{eq} and E_i are the Young's modulus of the equilibrium branch and the i th non-equilibrium branches respectively, w is the strain oscillation frequency used in dynamic mechanical analysis (DMA) test, $\tau_i(T)$ is the temperature dependent relaxation time for the i th branch and $E_l(T)$ is the loss modulus. The storage modulus given in Eq. (1) is taken as the elastic modulus of the fiber polymer and will be applied to calculate the elastic energy stored in SRASAs at various temperatures in the next section.

3.2. Theoretical modeling of the SRASA

In this section, the reconfigurable actuation of the SRASA is modeled based on the minimum potential energy principle (Reddy, 2017). The potential energy of the structure is introduced first. The strain tensor is constructed next by taking into account both bending and stretching. The elastic energies stored in both the orthotropic top layer and the homogeneous bottom layer are then obtained. The energy stored in the elastic cable and the work potential of the force are also calculated. Finally, the total potential energy is minimized to obtain the deformed state of the SRASA.

3.2.1. Potential energy of the structure

During actuation, the total potential energy $\Pi(T)$ of the SRASA consists of the elastic energy stored in the top layer $U_1(T)$, bottom layer U_2 and the cable $U_c(T)$, and the work potential of the force W_F :

$$\Pi(T) = U_1(T) + U_2 + U_c(T) + W_F(T), \quad (3)$$

where

$$U_i = \int \frac{1}{2} \varepsilon : \mathbb{C}_i : \varepsilon dV_i, i = 1, 2, \quad (4)$$

$$U_c(T) = \frac{1}{2} k_c(T) \times \Delta L_c^2, \quad (5)$$

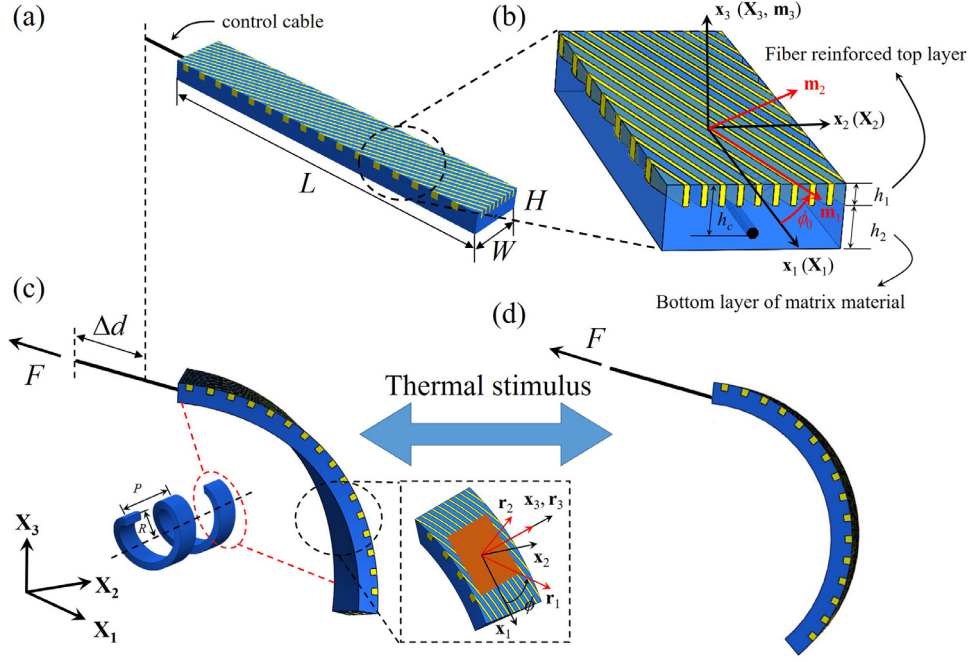


Fig. 1. (a) Schematic of an SRASA consisting of a top layer of anisotropic fiber reinforced composite and a bottom layer of elastomer. (b) Geometrical parameters and coordinate systems of the composite. (c) The SRASA deforms into a helical shape which can be characterized by the two basic parameters: pitch P and radius R . The inset of (c) illustrates a principle strain plane \mathbf{r}_1 - \mathbf{r}_2 where \mathbf{r}_3 axis coincides with the \mathbf{x}_3 axis and the \mathbf{r}_1 axis rotates counter-clockwise from \mathbf{x}_1 -axis by ϕ . (d) The deformed SRASA undergoes reversible reconfiguration subjected to a thermal stimulus.

$$W_F(T) = -\mathbf{F}_c \cdot \Delta_c. \quad (6)$$

Here $i = 1$ and 2 represent the top and bottom layer respectively. \mathbb{C}_i is the fourth-order elastic stiffness tensor and $\boldsymbol{\varepsilon}$ is the strain tensor. V_i is the volume. $k_c(T)$ and ΔL_c are the axial stiffness and elongation of the elastic control cable, respectively. The force vector is given by $\mathbf{F}_c = [F \ 0 \ 0]^T$ and the displacement vector by $\Delta_c = [\Delta d \ 0 \ 0]^T$. It should be noted that $k_c(T)$ depends on the temperature and thus U_c is a function of T . The second layer is an elastomeric layer whose elastic modulus remains a constant within our working temperature, and thus the elastic energy stored inside U_2 is independent of T .

3.2.2. Strain tensor in principal coordinates

In order to obtain the potential energy of the system, we first define the global coordinate system $(\mathbf{X}_1, \mathbf{X}_2, \mathbf{X}_3)$ and local coordinate system $(\mathbf{x}_1, \mathbf{x}_2, \mathbf{x}_3)$ as shown in Fig. 1. During the deformation of the SRASA, there always exists a principal coordinate system $(\mathbf{r}_1, \mathbf{r}_2, \mathbf{r}_3)$ where there is no shear strain. The \mathbf{r}_3 axis coincides with the \mathbf{x}_3 axis and we denote the angle from the \mathbf{x}_1 axis to the \mathbf{r}_1 axis as ϕ in the counter-clockwise direction. As in the classical plate theory, the strain tensor $\boldsymbol{\varepsilon}^{(r)}$ in the principal coordinate $(\mathbf{r}_1, \mathbf{r}_2, \mathbf{r}_3)$ can be obtained by superimposing the elastic bending strain $\boldsymbol{\varepsilon}_b^{(r)}$, an in-plane uniform stretching strain $\boldsymbol{\varepsilon}_s^{(r)}$ and a strain $\boldsymbol{\varepsilon}_{r_3}^{(r)}$ along \mathbf{r}_3 to allow for plane stress compatibility:

$$\boldsymbol{\varepsilon}^{(r)} = \boldsymbol{\varepsilon}_b^{(r)} + \boldsymbol{\varepsilon}_s^{(r)} + \boldsymbol{\varepsilon}_{r_3}^{(r)}, \quad (7)$$

where

$$\boldsymbol{\varepsilon}_b^{(r)} = \kappa_1 \mathbf{x}_3 \mathbf{r}_1 \otimes \mathbf{r}_1 + \kappa_2 \mathbf{x}_3 \mathbf{r}_2 \otimes \mathbf{r}_2, \quad (8)$$

$$\boldsymbol{\varepsilon}_s^{(r)} = e_{11} \mathbf{r}_1 \otimes \mathbf{r}_1 + e_{22} \mathbf{r}_2 \otimes \mathbf{r}_2, \quad (9)$$

$$\boldsymbol{\varepsilon}_{r_3}^{(r)} = (e_{33} + q \mathbf{x}_3) \mathbf{r}_3 \otimes \mathbf{r}_3. \quad (10)$$

Here e_{11} , e_{22} and e_{33} are the principal strains at $\mathbf{x}_3=0$ in the principal coordinates $(\mathbf{r}_1, \mathbf{r}_2, \mathbf{r}_3)$; κ_1 and κ_2 represent the principal curvatures along \mathbf{r}_1 and \mathbf{r}_2 respectively, and q denotes the gradient of the strain component along the \mathbf{r}_3 -axis.

3.2.3. Elastic energy in orthotropic top layer

The top layer is a fiber reinforced orthotropic composite by embedding aligning fibers inside the elastomeric matrix. In order to calculate the elastic energy stored in the top layer, we define material reference coordinates $(\mathbf{m}_1, \mathbf{m}_2, \mathbf{m}_3)$ [Fig 1(b)], where \mathbf{m}_1 is along the fiber orientation direction, \mathbf{m}_2 is perpendicular to the fiber orientation and \mathbf{m}_3 coincides with the \mathbf{x}_3 axis. The $(\mathbf{m}_1, \mathbf{m}_2, \mathbf{m}_3)$ coordinates can be formed by rotating the $(\mathbf{x}_1, \mathbf{x}_2, \mathbf{x}_3)$ coordinates by the fiber orientation angle ϕ_0 about the \mathbf{m}_3 axis. With respect to the orthonormal coordinates $(\mathbf{m}_1, \mathbf{m}_2, \mathbf{m}_3)$, the fourth-order compliance tensor of the orthotropic top layer can be expressed in matrix notation as:

$$\mathbf{C}_1(T) = \begin{bmatrix} \frac{1}{E_1(T)} & -\frac{\nu_{21}}{E_2(T)} & -\frac{\nu_{31}}{E_3(T)} & 0 & 0 & 0 \\ & \frac{1}{E_2(T)} & -\frac{\nu_{32}}{E_3(T)} & 0 & 0 & 0 \\ & & \frac{1}{E_3(T)} & 0 & 0 & 0 \\ & & & \frac{1}{G_{23}} & 0 & 0 \\ & & & & \frac{1}{G_{13}(T)} & 0 \\ \text{sym} & & & & & \frac{1}{G_{12}(T)} \end{bmatrix}^{-1}. \quad (11)$$

Here, $E_1(T)$, $E_2(T)$, $E_3(T)$ are the Young's moduli in the \mathbf{m}_1 , \mathbf{m}_2 and \mathbf{m}_3 directions, respectively. ν_{ij} is the Poisson's ratio, defined as the transverse strain in the j th direction corresponding to the axial strain in the i th direction. G_{23} , $G_{13}(T)$ and $G_{12}(T)$ are the shear moduli in the \mathbf{m}_2 - \mathbf{m}_3 , \mathbf{m}_1 - \mathbf{m}_3 and \mathbf{m}_1 - \mathbf{m}_2 planes, respectively. The nine parameters $E_1(T)$, $E_2(T)$, $E_3(T)$, G_{23} , $G_{13}(T)$, $G_{12}(T)$ and ν_{21} , ν_{31} , ν_{32} can be calculated from the Young's moduli $E_f(T)$, E_m , Poisson ratios ν_f and ν_m of the fiber and matrix materials, and the

fiber volume fraction V_f using the rule of mixture as shown in Supplementary Materials (Reddy, 2013).

$U_1(T)$ can then be calculated using Eq. (4) as:

$$U_1(T) = \int \frac{1}{2} \boldsymbol{\varepsilon}^{(m)} : \mathbb{C}_1 : \boldsymbol{\varepsilon}^{(m)} dV_1, \quad (12)$$

where $\boldsymbol{\varepsilon}^{(m)}$ is the strain tensor in the $(\mathbf{m}_1, \mathbf{m}_2, \mathbf{m}_3)$ coordinates which are obtained by transforming the strain tensor $\boldsymbol{\varepsilon}^{(r)}$ in the $(\mathbf{r}_1, \mathbf{r}_2, \mathbf{r}_3)$ coordinate system through an angle $\phi_0 - \phi$:

$$\varepsilon_{ij}^{(m)} = Q_{mi}^{(1)} Q_{nj}^{(1)} \varepsilon_{mn}^{(r)} \text{ and } \boldsymbol{\varepsilon}^{(m)} = \varepsilon_{ij}^{(m)} \mathbf{m}_i \otimes \mathbf{m}_j. \quad (13)$$

Here $Q_{ij}^{(1)}$ are the components of the transformation tensor $\mathbf{Q}^{(1)}$ with rotation angle $\phi_0 - \phi$. By substituting Eq. (11), and (13) into Eq. (12), U_1 can be obtained. Its complete expression is shown in Supplementary Materials.

3.2.4. Elastic energy in homogeneous bottom layer

Next, we calculate the elastic energy U_2 stored in the bottom layer. The bottom layer is made of an isotropic elastic material, and thus \mathbb{C}_2 can be written in matrix form in terms of its Young's modulus E_m and Poisson ratio ν_m as:

$$\mathbb{C}_2 = \frac{E_m}{(1 + \nu_m)(1 - 2\nu_m)} \times \begin{bmatrix} 1 - \nu_m & \nu_m & \nu_m & 0 & 0 & 0 \\ \nu_m & 1 - \nu_m & \nu_m & 0 & 0 & 0 \\ \nu_m & \nu_m & 1 - \nu_m & 0 & 0 & 0 \\ 0 & 0 & 0 & 1 - 2\nu_m & 0 & 0 \\ 0 & 0 & 0 & 0 & 1 - 2\nu_m & 0 \\ 0 & 0 & 0 & 0 & 0 & 1 - 2\nu_m \end{bmatrix}. \quad (14)$$

The elastic energy U_2 stored in the bottom layer can be derived based on Eq. (4) as shown in Supplementary Materials.

3.2.5. Elastic energy in cable

At the position $x_3 = -h_c$, the application of the external force F to the control cable results in the helical motion of the SRASA. The elongation ΔL_c of the control cable is given by $\Delta L_c = F/k_c(T)$, where the axial stiffness $k_c(T)$ is measured from an experiment (Supplementary Materials). Therefore, the elastic energy $U_c(T)$ stored in the deformed cable is

$$U_c(T) = F^2 / (2k_c(T)). \quad (15)$$

3.2.6. Work potential of force

The displacement Δd of the end of the cable that resulting from the external force F consists of the axial shortening of the SRASA and the elongation of the cable as:

$$\Delta d = \varepsilon_{11}(x_3 = -h_c) \cdot L + \Delta L_c. \quad (16)$$

Using $\varepsilon_{11}^{(r)}$, $\varepsilon_{22}^{(r)}$, and $\varepsilon_{33}^{(r)}$, we can calculate the strain components ε_{ij} of the strain tensor $\boldsymbol{\varepsilon}$ ($\boldsymbol{\varepsilon} = \varepsilon_{ij} \mathbf{x}_i \otimes \mathbf{x}_j$) in the $(\mathbf{x}_1, \mathbf{x}_2, \mathbf{x}_3)$ frame through the tensor coordinate transformation:

$$\varepsilon_{ij} = Q_{mi}^{(2)} Q_{nj}^{(2)} \varepsilon_{mn}^{(r)}. \quad (17)$$

Here $\mathbf{Q}^{(2)}$ is the transformation matrix with rotation angle $-\phi$. The normal strain component along the \mathbf{x}_1 -axis ε_{11} at $x_3 = -h_c$ in Eq. (17) is then given as:

$$\varepsilon_{11}(x_3 = -h_c) = (e_{11} - h_c \kappa_1) \cos^2 \phi + (e_{22} - h_c \kappa_2) \sin^2 \phi. \quad (18)$$

By substituting Eq. (18) and Δd in Eq. (16) into Eq. (6), the work potential W_F is:

$$W_F(T) = -LF[(e_{11} - h_c \kappa_1) \cos^2 \phi + (e_{22} - h_c \kappa_2) \sin^2 \phi] - F^2 / k_c(T). \quad (19)$$

3.2.7. Minimization of the potential energy

By substituting Eqs. (15), (19), (S6) and (S7) into Eq. (3), the total potential energy of the SRASA is obtained as a function of eight unknowns, i.e., $\Pi(T) = \Pi(\kappa_1, \kappa_2, q, e_{11}, e_{22}, e_{33}, \phi, T)$. Under a particular $T = T_p$, the SRASA arrives at the equilibrium when the total potential energy is minimized with respect to the other seven unknowns, which means

$$\begin{aligned} \frac{\partial \Pi(T = T_p)}{\partial \kappa_1} &= 0, \quad \frac{\partial \Pi(T = T_p)}{\partial \kappa_2} = 0, \quad \frac{\partial \Pi(T = T_p)}{\partial q} = 0, \\ \frac{\partial \Pi(T = T_p)}{\partial e_{11}} &= 0, \quad \frac{\partial \Pi(T = T_p)}{\partial e_{22}} = 0, \\ \frac{\partial \Pi(T = T_p)}{\partial e_{33}} &= 0, \quad \frac{\partial \Pi(T = T_p)}{\partial \phi} = 0. \end{aligned} \quad (20)$$

By solving the seven equations in Eq. (20) numerically, we can obtain the seven unknowns to express the total potential energy at any temperature. After the seven unknowns $\kappa_1, \kappa_2, q, e_{11}, e_{22}, e_{33}$ and ϕ are obtained, the deformed SRASA can be reconstructed. The centerline of the deformed SRASA can be regarded as a helix with pitch P and radius R , where (Wang et al., 2018a)

$$|P| = 2\pi \frac{(\kappa_1 - \kappa_2) \sin 2\phi}{\kappa_1^2 + \kappa_2^2 + (\kappa_1^2 - \kappa_2^2) \cos 2\phi}, \quad (21)$$

and

$$R = \frac{\kappa_1 + \kappa_2 + (\kappa_1 - \kappa_2) \cos 2\phi}{\kappa_1^2 + \kappa_2^2 + (\kappa_1^2 - \kappa_2^2) \cos 2\phi}. \quad (22)$$

In Eq. (21), $|P|$ represents the magnitude of P . By using coordinate transformation, the coordinates of points along the width and thickness direction of the deformed SRASA can be obtained. The deformed shapes are plotted using the software ParaView (Ayachit, 2015).

4. Validation of the model

In this section, the theoretical model is validated by experiments. The modulus change of the fiber material on temperature is verified first, and the deformation of SRASA predicted by the theory is compared with experiments next. The SRASAs are fabricated using a commercial multimaterial 3D printer (Stratasys, Connex 500). The dimensions are $L = 50$ mm, $W = 8$ mm, $H = 3$ mm, $h_1 = 1$ mm, $h_2 = 2$ mm and $h_c = 2.25$ mm. SRASAs with seven fiber orientation angles $\phi_0 = 0^\circ, 15^\circ, 30^\circ, 45^\circ, 60^\circ, 75^\circ$ and 90° are printed. The fiber volume fraction v_f of the top fiber reinforced layer is 33%. The base compliant material, TangoPlus, is used as the matrix material, and the base shape memory polymer, VeroClear, is used as the fiber material. Different from many previous studies (Ge et al., 2014, 2016b; Wang et al., 2020) where the VeroClear was used as a shape memory polymer, this work utilizes the stiffness variation over temperature of VeroClear (Zhang et al., 2019) to impart the capability of switching in-plane and helical bending modes into one 3D printed soft actuator. Stress relaxation tests, DMA analysis and uniaxial tensile tests for the SMP fibers and nylon cable are conducted and the detailed information can be found in Supplementary Materials.

4.1. Material characterization results

The experimental and theoretical fitted storage modulus and the $\tan \delta$ curve of the VeroClear are shown as the black solid curve and red dashed curves in Fig. 2 respectively. It can be seen that the theoretically estimation could the experimental data. Fitted parameters can be found in Table S1 in Supplementary Materials.

Uniaxial tensile tests on VeroClear samples at various temperature $T = 25, 30, 35, 40, 45, 50, 60, 70$ and 80°C are conducted and

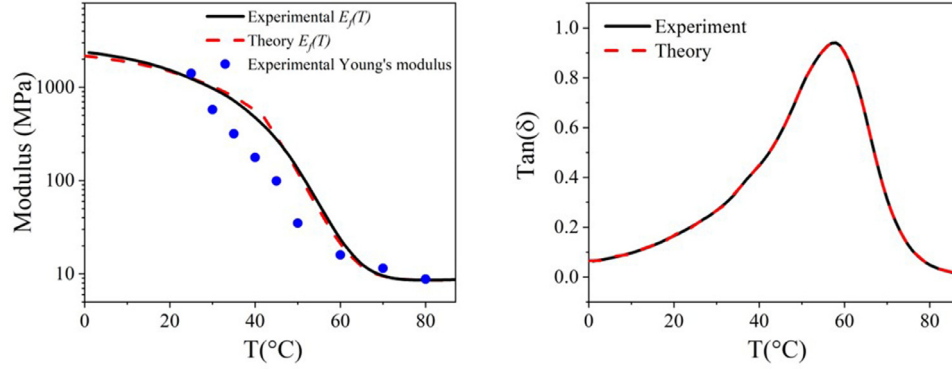


Fig. 2. (a) Variation of the experimental (black solid) and theoretical (red dashed) curves of the storage modulus $E_f(T)$ of the SMP fiber with temperature. The uniaxial tensile tested Young's modulus at various temperature $T = 25, 30, 35, 40, 45, 50, 60, 70$ and 80 °C are also shown as blue markers. (b) Comparison between the experimental and theoretical curves of $\tan\delta$.

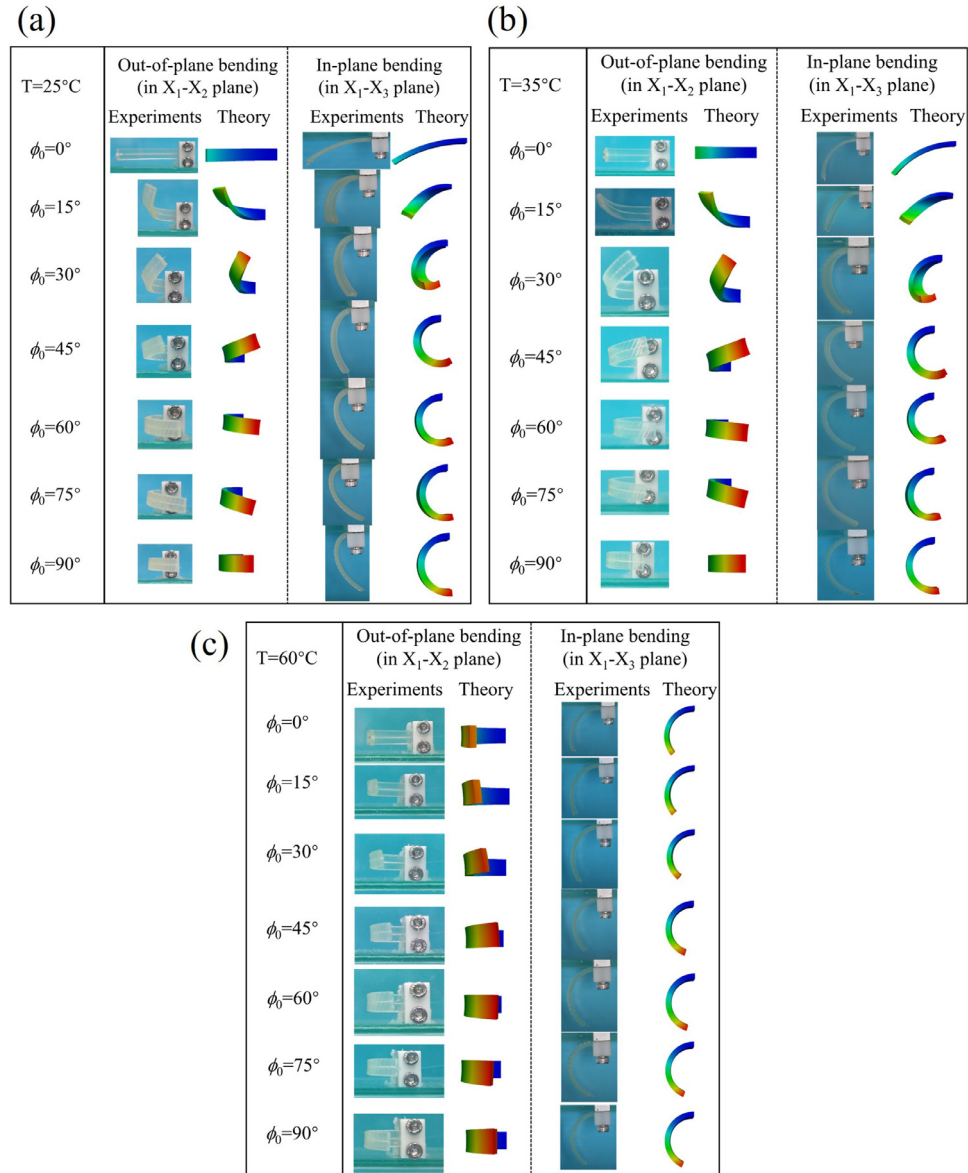


Fig. 3. The comparisons of the top and front views of the SRASA with $\phi_0 = 0^\circ, 15^\circ, 30^\circ, 45^\circ, 60^\circ, 75^\circ$ and 90° between experiments (first and third columns) and theoretical simulations (second and fourth columns) at (a) $T = 25$ °C, (b) $T = 35$ °C and (c) $T = 60$ °C.

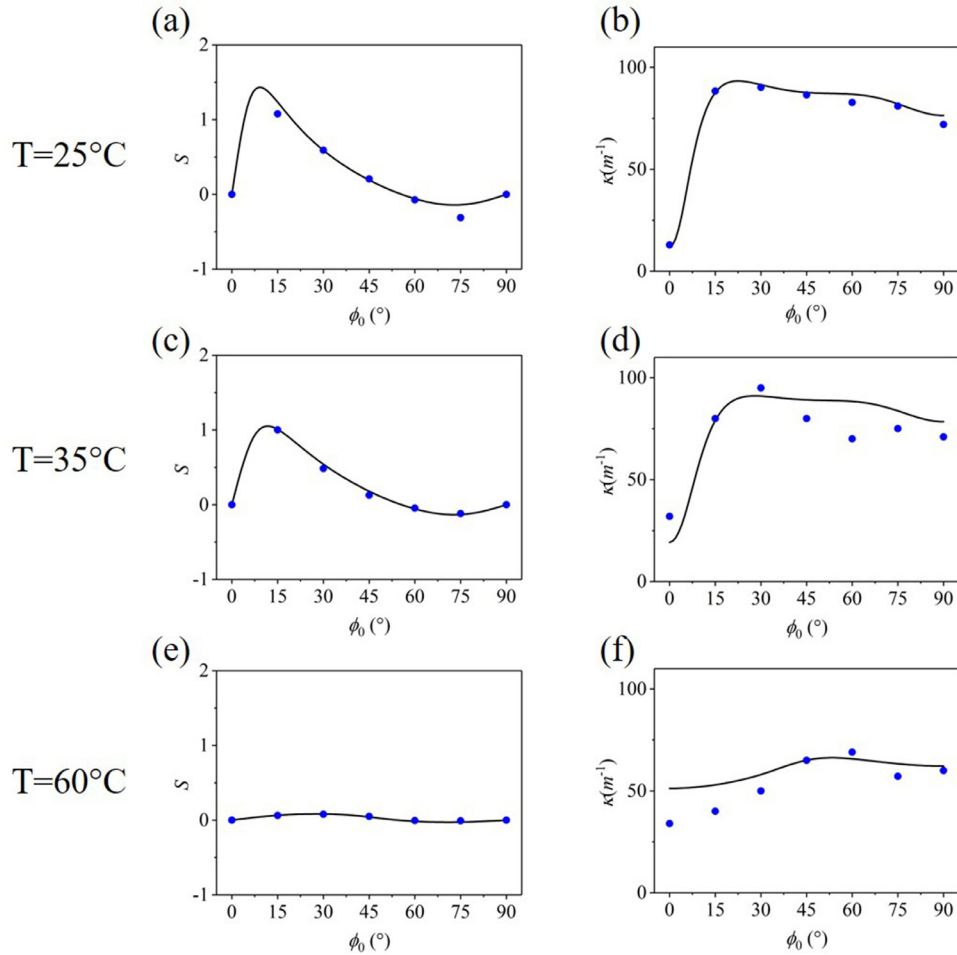


Fig. 4. The dependence of slope S and curvature κ on fiber orientation angle ϕ_0 of a deformed SRASA (Experimental results: blue circle. Model predictions: black solid curves) at different temperatures $T = 25^\circ\text{C}$, 35°C and 60°C .

the corresponding Young's modulus are plotted as blue markers in Fig. 2(a). It can be seen that the storage modulus $E_f(T)$ which is obtained by applying a sinusoidal strain compares reasonably with the Young's modulus which is obtained by applying a uniaxial tensile strain. Thus, $E_f(T)$ can be used as the Young's modulus of the SMP fiber and to study the continuous temperature dependent behavior of the SRASA.

4.2. Comparison of the theoretical and experimental SRASA actuation tests

The SRASA actuation test results for $T = 25^\circ\text{C}$ with $\Delta d = 10\text{ mm}$, $T = 35^\circ\text{C}$ with $\Delta d = 15\text{ mm}$, and $T = 60^\circ\text{C}$ with $\Delta d = 15\text{ mm}$ for $\phi_0 = 0^\circ, 15^\circ, 30^\circ, 45^\circ, 60^\circ, 75^\circ$ and 90° are shown in Fig. 3. During the tests, the soft actuators are placed in a water tank. In the heating process, the temperature of the water was slowly increased from room temperature by a heating source, and measured by a temperature sensor. At $T = 25^\circ\text{C}$, the SRASA shows both in-plane and out-of-plane bending, except for $\phi_0 = 0^\circ$ and 90° . The out-of-plane bending is towards the positive \mathbf{X}_2 direction for smaller ϕ_0 ($\leq 45^\circ$) and negative \mathbf{X}_2 direction for larger ϕ_0 ($\geq 60^\circ$). The SRASA shows similar behavior at $T = 35^\circ\text{C}$ as those at $T = 25^\circ\text{C}$. However, as the temperature increases the magnitude of the out-of-plane bending decreases, because the Young's modulus of the fiber decreases and thus leads to the decrease of the anisotropy. At $T = 60^\circ\text{C}$, almost all SRASAs exhibit only in-plane bending due to the further decrease of the anisotropy. The corre-

sponding theoretical predicted 3D shapes are shown next to the experimental shapes. The dependence of the fiber Young's modulus is obtained from Eq. (1) and Section S1.2 in the Supplementary Materials, while the Young's modulus of the matrix is chosen as $\sim 0.6\text{ MPa}$ (Wang et al., 2018a). The Poisson's ratios are chosen as $\nu_f = 0.48$ for fiber and 0.46 for matrix. It can be observed that the theoretical predictions agree well with the experiments.

Next, we quantitatively compare the experiments and the theoretical results. It can be seen that the centerline of the deformed SRASAs can be regarded as a helix with pitch P and radius R (Fig. 1(c)). Or we could use another set of parameters, the slope $S = P/(2\pi R)$ and curvature $\kappa = 1/R$, to represent the helix. The deformed SRASAs with mainly in-plane bending can be regarded as a special case of a helix with $S = 0$. The experimental S and κ are then obtained by fitting the parametric function of a helix with the experimental coordinates of the centerline of each deformed SRASA in the $\mathbf{X}_1\text{-}\mathbf{X}_2$ and $\mathbf{X}_1\text{-}\mathbf{X}_3$ planes simultaneously. Detailed information about obtaining the experimental S and κ can be found in Supplementary Material.

Fig. 4 shows the comparison of the experimental (blue markers) and theoretical (black curves) of S and κ for the SRASAs shown in Fig. 3. It can be seen that both the theoretical S and κ agree reasonably with the experiments. S exhibits similar trend at different temperatures while varying ϕ_0 . S is 0 at $\phi_0 = 0^\circ$ and 90° at all different temperatures, which means that the SRASAs exhibit only in-plane bending. At $\phi_0 \sim 15^\circ$, the SRASAs deform with the largest S . With the increase of ϕ_0 , S decreases gradually until it

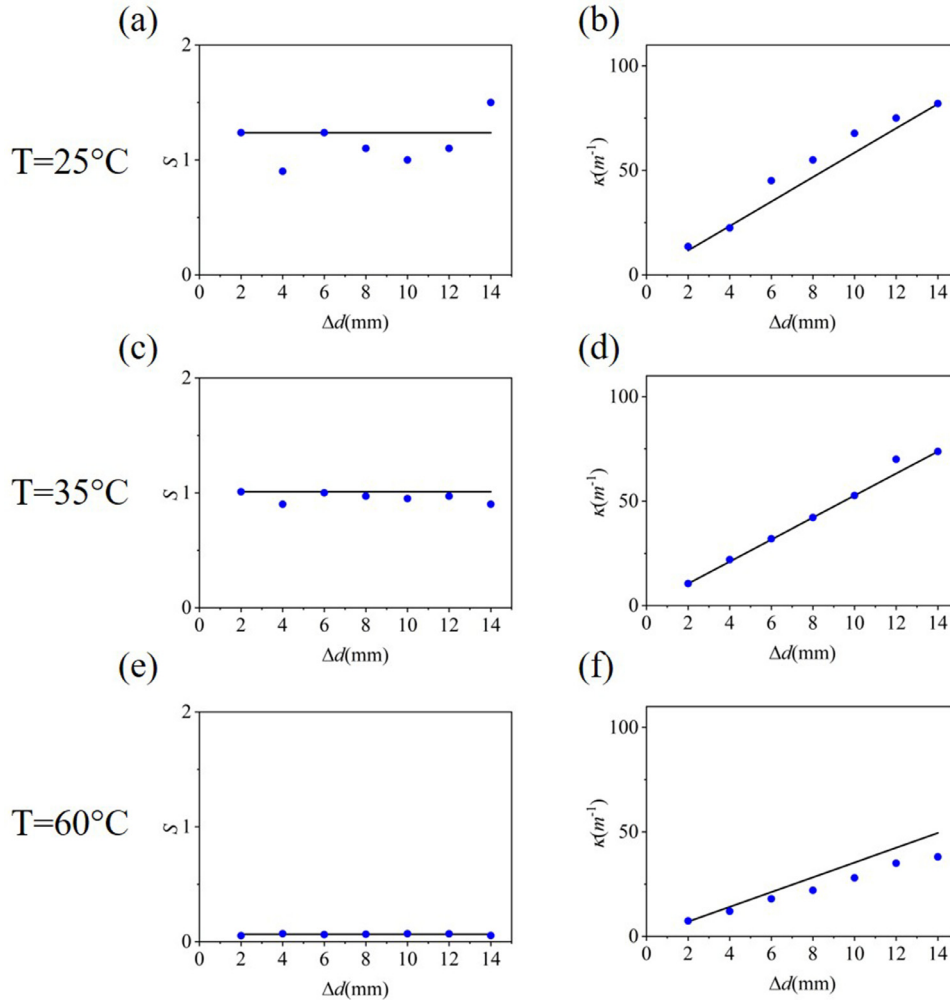


Fig. 5. The effect of the pulling distance Δd of the control cable on the slope S and curvature κ of a deformed SRASA (Experimental results: blue circle. Model predictions: black solid curves) at different temperatures $T = 25^\circ\text{C}$, 35°C and 60°C .

reaches zero at around $\phi_0 = 60^\circ$ and its negative maximum at $\phi_0 = 75^\circ$, before going back to 0 again at $\phi_0 = 90^\circ$. The magnitudes of S decrease as the temperature increases, which can be easily seen from the deformed shapes at $T = 60^\circ\text{C}$ in Fig. 3, where the SRASAs are bending-dominated ($S \approx 0$). κ is at its minimum at $\phi_0 = 0^\circ$ where the fibers are aligned along the cable direction and the SRASA has highest bending modulus. At low temperature ($T = 25^\circ\text{C}$ and 35°C), κ increases rapidly at $\phi_0 = 15^\circ$ and keeps at relatively larger values. At high temperature ($T = 60^\circ\text{C}$), κ increases slowly and reaches its maximum at $\phi_0 = 60^\circ$.

Fig. 5 shows the experimental and theoretical S and κ against the pulling distance Δd of the cable at $T = 25^\circ\text{C}$, 35°C and 60°C with $\phi_0 = 15^\circ$, respectively. Under all three temperatures, κ is linearly proportional to Δd , while S is a constant with Δd . It indicates that S is an intrinsic property of the SRASAs that depends only on material and geometric parameters and is independent of the loading parameters. It should be noted that the force F generated by the cable is also proportional to Δd , which are not shown here.

5. Numerical results

In this section, the validated theoretical model is used to predict the actuation behaviors of the SRASAs. The effects of temperature and fiber orientation are investigated.

5.1. Effect of temperature T

Figs. 6(a) and (b) show an overview of the effects of the ambient temperature T and fiber orientation angle ϕ_0 on S and κ of the deformed helical shape. In particular, Figs. 6(c) and (d) plot S and κ as a function of temperature T for different fiber orientations $\phi_0 = 0^\circ, 15^\circ, 30^\circ, 45^\circ, 60^\circ, 75^\circ$ and 90° . Here the external force is fixed at $F = 16\text{ N}$. The control fiber stiffness is assumed to be infinite. As T increases, the magnitude of the slopes at all fiber orientations decreases. This is because the fiber's Young's modulus decreases with the increase of the temperature and therefore the anisotropy of the SRASA decreases. Thus the deformed shape of the SRASA will change from twist-dominated mode (inset (i) and (iv)) at low temperature to moderate twisting mode at intermediate temperature (inset (ii) and (v)), to bending-dominated mode at high temperature (inset (iii) and (vi)). In most cases, as T increases, κ also increases as shown in Fig. 6(d) because the SRASA becomes softer and thus it bends more under the same applied force. In contrast, a minimum of κ exists for $\phi_0 = 15^\circ$ and 30° at $T = 45^\circ\text{C}$ and $T = 52^\circ\text{C}$, respectively.

5.2. Effect of fiber orientation ϕ_0

Next the effect of ϕ_0 is studied as shown in Figs. 6(e) and (f), where the S and κ are plotted against ϕ_0 at $T = 10, 20, 30, 40, 50$ and 60°C . The slope increases from 0 at $\phi_0 = 0^\circ$ rapidly un-

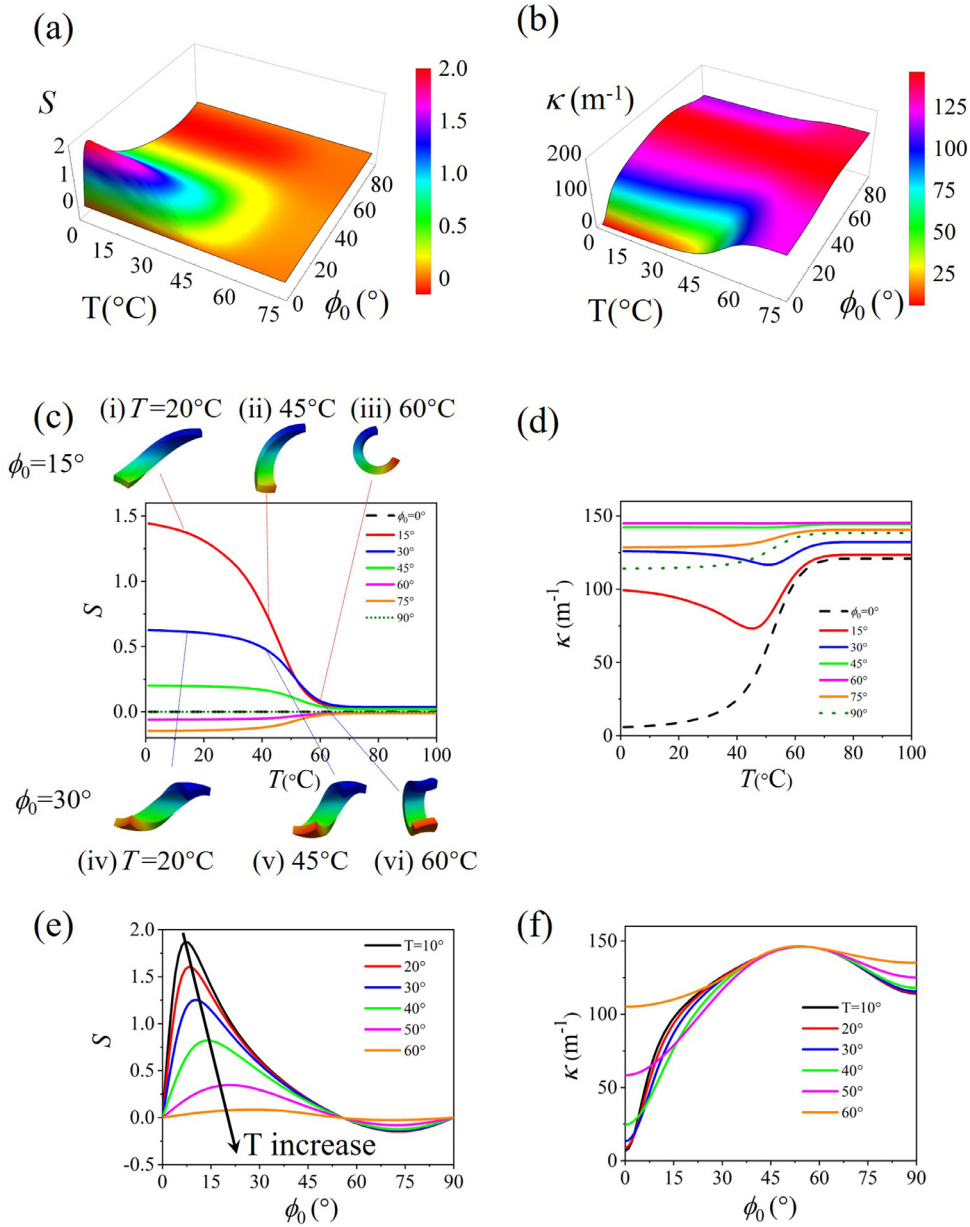


Fig. 6. The 3D plot of the dependence of (a) Slope S and (b) curvature κ on temperature and ϕ_0 . The dependence of (c) the slope S and (d) curvature κ on temperature for different fiber orientation angles $\phi_0 = 0^\circ, 15^\circ, 30^\circ, 45^\circ, 60^\circ, 75^\circ$ and 90° ; insets shows the deformed shapes for $\phi_0 = 15^\circ$ and 30° at $T = 20^\circ\text{C}, 45^\circ\text{C}$ and 60°C . The dependence of (e) slope S and (f) curvature κ as a function of ϕ_0 at different $T = 10^\circ\text{C}, 20^\circ\text{C}, 30^\circ\text{C}, 40^\circ\text{C}, 50^\circ\text{C}$ and 60°C .

til it reaches its maximum value at $\phi_0 \approx 10\text{--}30^\circ$ depending on the temperature, and then decreases to 0 at a critical $\phi_c \approx 55^\circ$. As ϕ_0 increases again, the slope changes to a negative value and reaches its negative maximum value at $\phi_0 \approx 70^\circ$, and the slope subsequently goes back to 0 at $\phi_0 = 90^\circ$. The change of the sign of slope means that the out-of-plane bending direction of the soft actuator changes. Similar behaviors of changing direction crossing the critical fiber orientation $\phi_c = 55^\circ$ were also reported in McKibben artificial muscles (Chou et al., 1996; Wang et al., 2017), fiber reinforced pneumatic soft actuators (Bishop-Moser and Kota, 2015; Connolly et al., 2017), arterial tissues (Horgan and Murphy, 2018a, 2018b) and tendons (Bydder et al., 2007). κ increases first as the fiber orientation increases and reaches its maximum at $\phi_0 \approx 55^\circ$ and then reduces slowly as shown in Fig. 6(f).

5.3. Shape with maximum slope S_{max} at different T

S indicates the twisting/out-of-plane bending of the SRSA. For a certain S , the maximum slope S_{max} indicates the maximum twisting a soft actuator can achieve by adjusting the fiber orientation. From Fig. 6(e), it can be seen that the ϕ_0 associated with S_{max} varies for different temperatures. It would be interesting to see how the temperature affects the S_{max} of the SRSA and the corresponding ϕ_0 . Fig. 7 shows the maximum value of the slope S_{max} and the corresponding ϕ_0 at different temperatures. The S_{max} decreases monotonically with the temperature due to the lower anisotropy at high temperature. The corresponding ϕ_0 increases monotonically with the temperature from $\phi_0 = 6^\circ$ at $T = 0^\circ\text{C}$ to $\phi_0 = 32^\circ$ at $T = 80^\circ\text{C}$. The inset figures show the deformed shapes with S_{max} at $T = 20, 40$ and 60°C under a fixed force $F = 16\text{ N}$. At

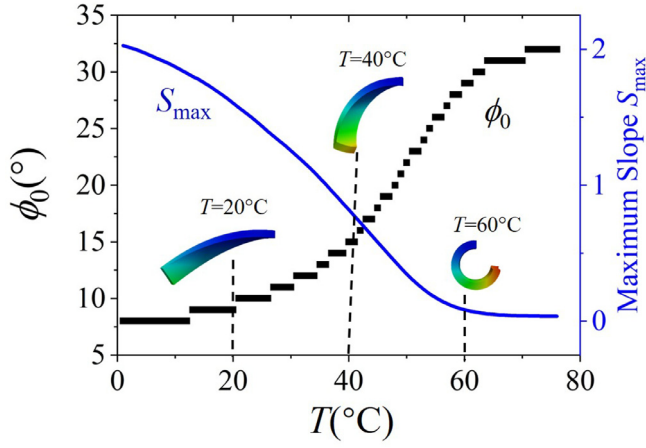


Fig. 7. The dependence of the maximum slope S_{\max} and its corresponding ϕ_0 on T . Insets show deformed shapes of soft actuators with maximum slope at $T = 20$, 40 and 60 °C.

$T = 20$ °C, S is large. However, the magnitude of the twisting and bending are both small due to the large E_f at low temperature. At $T = 40$ °C, the SRASA bends and twists more than that at $T = 20$ °C, and therefore provides a better actuation. This larger bending and twisting results from the decrease of E_f with increasing temperature. As $T > 60$ °C, the SRASA becomes highly bending-dominated due to the decrease of material inhomogeneity. It should be noted that ϕ_0 is restricted to be an integer in Fig. 7 which makes the curve of ϕ_0 discontinuous.

6. Bio-inspired design and discussion

We further demonstrate an application uniquely enabled by the helical deformation of the SRASAs. Some coral polyps use twisting motion to capture plankton and even small fish swimming by. Compared to the bending motion, the helical motion provides larger and tighter coverage. The overlap at the bottom of the gripper can also provide large forces to prevent the prey from escaping. Inspired by the twisting motion of the coral polyps, six-handed grippers are designed with different fiber orientations and work

Table 1

Forces applied on each SRASA in the six-hand soft grippers in Fig. 8.

	$\phi_0 = 15^\circ$	$\phi_0 = 30^\circ$	$\phi_0 = 45^\circ$	$\phi_0 = 90^\circ$
$T = 25$ °C	16 N	6.4 N	2.9 N	3.2 N
$T = 60$ °C	3.4 N	3.2 N	2.9 N	2.6 N

on different ambient temperatures. The gripper consists of a cap and six identical SRASAs. The theoretical predicted deformation of the six-hand gripper is shown in Fig. 9. The corresponding forces applied on each SRASAs are shown in Table 1. It can be observed that gripper with $\phi_0 = 30^\circ$ and $T = 25$ °C can provide a better capacity of catching and grabbing. Its theoretical performance with increasing applied forces is shown in Supplementary Movie S1. At $\phi_0 = 15^\circ$, the SRASAs show large helical deformation, but its bottom cannot be fully covered. As the ambient temperature increases, the anisotropy of the SRASAs decreases and all the grippers exhibit pure bending grabbing. In order to prove the capacity of the gripper with $\phi_0 = 30^\circ$, experiments were conducted. We 3D printed the cap and SRASAs separately and then assemble them together. As shown in Fig. 9 and Supplementary Movie S2, the soft gripper could catch and releasing a live goldfish in water by pulling and releasing the control cable. The intrinsic softness of the soft actuator enables its safe interaction with goldfish and without causing any harm to it. Compared to the in-plane bending deformation, the SRASAs in the twisting mode could arrange more efficiently in space to avoid conflict and generate larger coverage areas.

Most of the previously proposed reconfigurable 3D printed structures are based on the actuation of built-in strain/stress (Ding et al., 2018, 2017) or the shape memory effect of the polymers (Ge et al., 2014, 2013, 2016a), which are generally one-way actuation and not reversible. The built-in strain/stress is usually generated by the layer by layer deposition or photopolymerization during 3D printing. For example, a direct 4D printing method for active composite materials is proposed and the composite can be programmed with the built-in compressive strain during photopolymerization (Ding et al., 2017). The other way of 3D reconfiguration is by using the polymers' shape memory effect cycle, where various of 3D printed reconfigurable structures are pro-

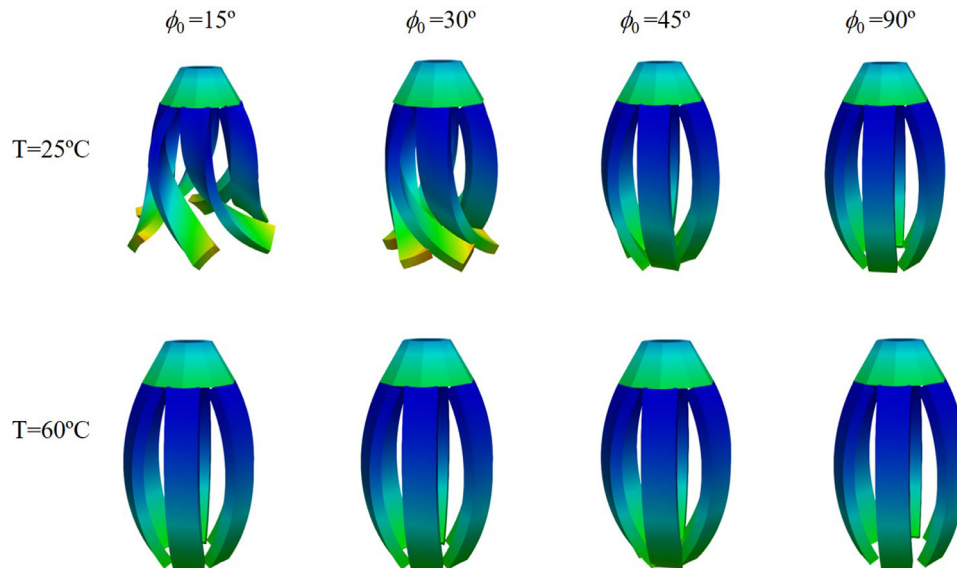


Fig. 8. Theoretical predicted deformation of the six-hand grippers made from SRASAs with various temperatures and fiber orientation angles. The corresponding forces are shown in Table 1.

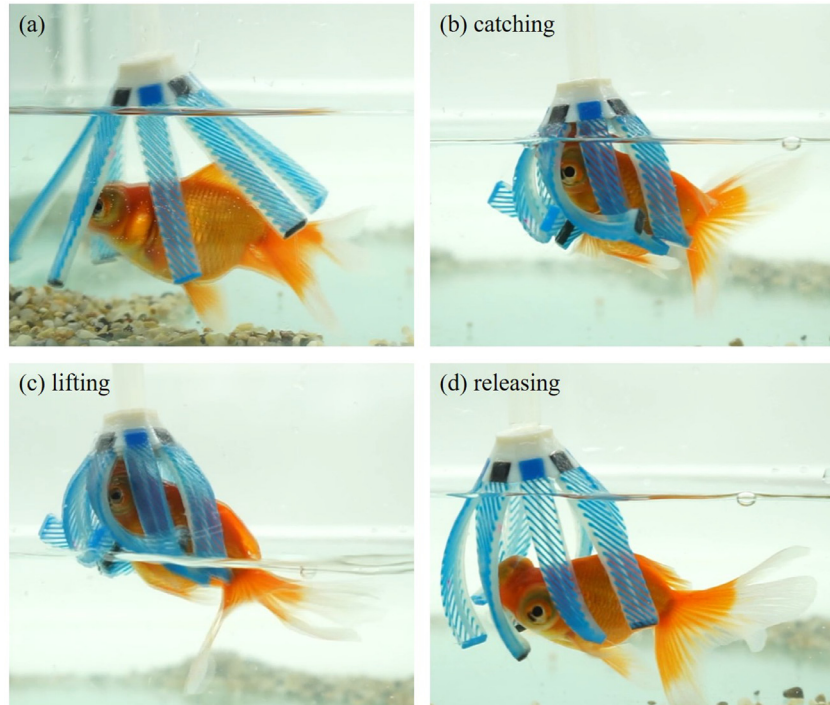


Fig. 9. A six-handed soft gripper catches, lifts and releases a live goldfish. The twisting motion provides more efficient catching ability. The geometrical parameters used for each SRASA are: $L = 50$ mm, $W = 8$ mm, $H = 3$ mm, $h_1 = 1$ mm, $h_2 = 2$ mm, $h_c = 2.5$ mm and $\phi_0 = 30^\circ$.

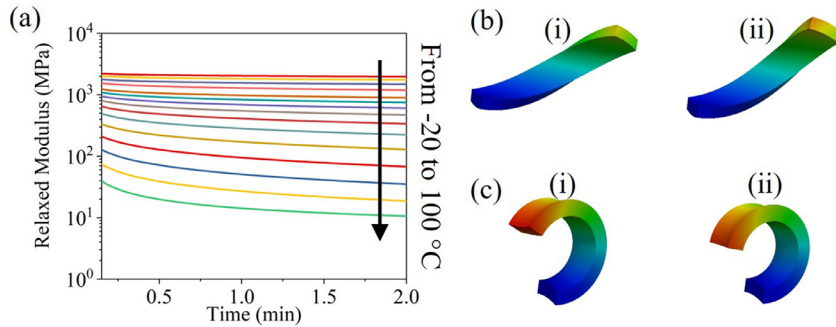


Fig. 10. Stress relaxation phenomenon of the SRASA. (a) The relaxed modulus changes with time in 2 min after loading for the fiber materials from -20°C to 100°C in stress relaxation tests. (b) The deformed shapes of the SRASA (i) immediately after the actuation and (ii) 2 min later after the actuation at $T = 25^\circ\text{C}$. (c) The deformed shapes of the SRASA (i) immediately after the actuation and (ii) 2 min later after the actuation at $T = 60^\circ\text{C}$. In both (b) and (c), $\phi_0 = 15^\circ$ and the actuation force is 16 N.

posed (Ge et al., 2016a; Yang et al., 2019). In our work, the reconfigurable behavior of the 3D printed SRASAs is reversible by using the actuation of both the control cable and the temperature-dependent modulus of the fiber. By adjusting the thermal stimulus, the deformed SRASAs can achieve reversible and continuous shape transitions between twisting-dominated and bending-dominated states.

It should be noted that linear elasticity theory and small deformation theory are used in this work, instead of nonlinear elasticity theory and finite deformation theory. The overall deformation of the SRASAs seems to be large, but the local strain is relatively small. For example, the axial strains of the SRASAs in this work are generally smaller than 5%. Furthermore, the moduli of the TangoPlus matrix and VeroClear SMP fiber is in the order of MPa to GPa, which is considerably larger than “ultrasoft” materials such as hydrogels with modulus generally in the order of kPa. The comparison between theoretical and experimental results show that linear elasticity with a small deformation approximation gives reasonable agreements. Nonlinear elasticity and finite deformation theory, although appropriate, lead to mathematical intractability, and

the complicated configurations of the materials will render numerical simulations difficult.

As shown in the stress relaxation tests in Fig. S1, the modulus of the fiber material decreases with time when a fixed strain is applied. This creep effect of the fiber may affect the shapes of the soft actuators. Fig. 10 shows the effect of stress relaxation on the deformation of the SRASA. Fig. 10(a) plots the modulus change of the fibers with time in 2 min in the stress relaxation tests. It can be seen that the relaxed modulus decreases faster initially and then approaches a constant value with time. For example, the fiber modulus is 877 MPa immediately after the actuation and 470 MPa at 2 min after the actuation at $T = 25^\circ\text{C}$. The modulus is 20 MPa and 8 MPa at immediately and 2 min after the actuation at $T = 60^\circ\text{C}$, respectively. By using the fiber modulus at various time after loading, the corresponding deformed shapes can be obtained. Fig. 10(b) plots the deformed shapes of the SRASA (i) immediately and (ii) 2 min after the actuation at $T = 25^\circ\text{C}$. Similarly, the deformed shapes of the SRASA (i) immediately and (ii) 2 min after the actuation at $T = 60^\circ\text{C}$ are plotted in Fig. 10(c). For both SRASAs, $\phi_0 = 15^\circ$ and the actuation force is 16 N. It can be

seen that there are some minor changes in the deformed shapes with time after the actuation. But it is not obvious in the experiments.

In-plane bending actuation, as a special case of helical deformation actuation, has already been used in many areas such as in soft wearable assistive gloves, bionic hand and in the locomotion of the soft robotics, due to their advantage of easy to fabricate, easy to model and easy to control (de Payrebrune and O'Reilly, 2016; Ge et al., 2018; Mosadegh et al., 2014; Wang et al., 2019). For example, soft wearable assistive gloves are designed by using fabric-based bending actuators that can assist finger flexion for brachial plexus injury patients (Ge et al., 2020). Tendon-driven bending soft actuators are used to fabricate bionic hand (Kim et al., 2016). Bending soft actuators are also used in the actuation of soft robotics, such as the locomotion of fluidic soft robots and the swimming of the Manta robot (Shepherd et al., 2011; Suzumori et al., 2007). Soft actuators with helical deformation can not only provide the normal bending actuation, but also a friction force on the transverse direction. Therefore, it greatly broadens the application scope of soft actuators.

The position of the control cable also plays a vital role in programming the deformation of SRASAs. If the cable works on the neutral axis of the composite, it will exhibit only twisting deformation around its neutral axis. By placing the cable above or below the neutral axis, the bending direction of the SRASAs can be controlled.

7. Conclusion

In summary, we have designed a programmable 3D printed soft actuator that exhibits reconfigurable deformations, in particular helical deformation, under thermal stimulus. A theoretical framework based on minimum potential energy is proposed to model the deformation of the SRASA, in which the dependence of the mechanical behaviors of the SMP fiber material on temperature is characterized by a thermomechanical multi-branch model. A set of stress relaxation tests were conducted to identify the SMP fiber's material parameters, which consequently enables the model to reproduce the experimentally observed reconfigurable actuation behaviors of the SRASAs successfully. Both the fiber orientation angles and the ambient temperature determine the anisotropy of the SRASAs, which control the deformation of the programmable, reconfigurable soft actuators. Finally, a bio-inspired six-handed soft gripper is designed, modeled and manufactured to catch a living fish in water using the helical deformation. The concept of adjusting anisotropy to generate reconfigurable structures and the design guidelines provided by the theoretical model provide the possibility for future applications such as soft robotics, metamaterials and medical devices.

Declaration of Competing Interest

None

Acknowledgements

D.W. acknowledges the support by the National Natural Science Foundation of China (Grant No. 51905336), the Shanghai Sailing Program (19YF1423000) and the Digital Manufacturing and Design Centre at SUTD. Q.G. acknowledges the support by the Centers for Mechanical Engineering Research and Education at MIT and SUSTech. B.Z. acknowledges National Natural Science Foundation of China (No. 51903210), National Science Basic Research Program of Shaanxi (Program No. 2020JQ-174), the Fundamental Research Funds for the Central Universities (No. 31020190QD015). G.Y. G. ac-

knowledges the support by the National Natural Science Foundation of China (Grant No. 91848204).

Supplementary materials

Supplementary material associated with this article can be found, in the online version, at doi:10.1016/j.ijsolstr.2020.04.028.

Reference

- Ayachit, U., 2015. The Paraview guide: a Parallel Visualization Application. Kitware, Inc.
- Bertoldi, K., Vitelli, V., Christensen, J., van Hecke, M., 2017. Flexible mechanical metamaterials. *Nat. Rev. Mater.* 2, 17066.
- Bishop-Moser, J., Kota, S., 2015. Design and modeling of generalized fiber-reinforced pneumatic soft actuators. *IEEE Trans. Rob.* 31, 536–545.
- Bydder, M., Rahal, A., Fullerton, G.D., Bydder, G.M., 2007. The magic angle effect: a source of artifact, determinant of image contrast, and technique for imaging. *J. Magn. Reson. Imaging* 25, 290–300.
- Cestari, M., Sanz-Merodio, D., Arevalo, J.C., Garcia, E., 2014. ARES, a variable stiffness actuator with embedded force sensor for the ATLAS exoskeleton. *Industrial Robot: Int.J.* 41, 518–526.
- Chou, C.-P., Hannaford, B., 1996. Measurement and modeling of McKibben pneumatic artificial muscles. *IEEE Trans. Rob.* 12, 90–102.
- Connolly, F., Walsh, C.J., Bertoldi, K., 2017. Automatic design of fiber-reinforced soft actuators for trajectory matching. *Proc. Natl. Acad. Sci.* 114, 51–56.
- Dawson, C., Vincent, J.F., Rocca, A.-M., 1997. How pine cones open. *Nature* 390, 668.
- de Payrebrune, K.M., O'Reilly, O.M., 2016. On constitutive relations for a rod-based model of a pneu-net bending actuator. *Extreme Mech. Lett.* 8, 38–46.
- Ding, Z., Weeger, O., Qi, H.J., Dunn, M.L., 2018. 4D rods: 3D structures via programmable 1D composite rods. *Mater. Des.* 137, 256–265.
- Ding, Z., Yuan, C., Peng, X., Wang, T., Qi, H.J., Dunn, M.L., 2017. Direct 4D printing via active composite materials. *Sci. Adv.* 3, e1602890.
- Forterre, Y., Skotheim, J.M., Dumais, J., Mahadevan, L., 2005. How the Venus flytrap snaps. *Nature* 433, 421.
- Ge, L., Chen, F., Wang, D., Zhang, Y., Han, D., Wang, T., Gu, G., 2020. Design, modeling, and evaluation of fabric-based pneumatic actuators for soft wearable assistive gloves. *Soft Robotics*.
- Ge, L., Dong, L., Wang, D., Ge, Q., Gu, G., 2018. A digital light processing 3D printer for fast and high-precision fabrication of soft pneumatic actuators. *Sens. Actuators A* 273, 285–292.
- Ge, Q., Dunn, C.K., Qi, H.J., Dunn, M.L., 2014. Active origami by 4D printing. *Smart Mater. Struct.* 23, 094007.
- Ge, Q., Qi, H.J., Dunn, M.L., 2013. Active materials by four-dimension printing. *Appl. Phys. Lett.* 103, 131901.
- Ge, Q., Sakhaei, A.H., Lee, H., Dunn, C.K., Fang, N.X., Dunn, M.L., 2016a. Multimaterial 4D printing with tailorable shape memory polymers. *Sci. Rep.* 6, 31110.
- Ge, Q., Serjouei, A., Qi, H.J., Dunn, M.L., 2016b. Thermomechanics of printed anisotropic shape memory elastomeric composites. *Int. J. Solids Struct.* 102, 186–199.
- Gerbode, S.J., Puzey, J.R., McCormick, A.G., Mahadevan, L., 2012. How the cucumber tendril coils and overwinds. *Science* 337, 1087–1091.
- Ghosh, P., Rao, A., Srinivasa, A.R., 2013. Design of multi-state and smart-bias components using shape memory alloy and shape memory polymer composites. *Mater. Des.* 44, 164–171.
- Gorissen, B., Vincentie, W., Al-Bender, F., Reynaerts, D., De Volder, M., 2013. Modeling and bonding-free fabrication of flexible fluidic microactuators with a bending motion. *J. Micromech. Microeng.* 23, 045012.
- Gu, G., Zou, J., Zhao, R., Zhao, X., Zhu, X., 2018. Soft wall-climbing robots. *Science Robotics* 3, eaat2874.
- Hannan, M.W., Walker, I.D., 2003. Kinematics and the implementation of an elephant's trunk manipulator and other continuum style robots. *J. Robot. Syst.* 20, 45–63.
- Hao, Y., Wang, T., Ren, Z., Gong, Z., Wang, H., Yang, X., Guan, S., Wen, L., 2017. Modeling and experiments of a soft robotic gripper in amphibious environments. *Int. J. Adv. Rob. Syst.* 14, 1729881417707148.
- Horgan, C., Murphy, J., 2018a. Magic angles and fibre stretch in arterial tissue: insights from the linear theory. *J. Mech. Behav. Biomed. Mater.* 88, 470–477.
- Horgan, C., Murphy, J., 2018b. Magic angles for fibrous incompressible elastic materials. *Proceedings of the Royal Society A: Mathematical, Physical Engineering Sciences* 474, 20170728.
- Janke, L., Czaderski, C., Motavalli, M., Ruth, J., 2005. Applications of shape memory alloys in civil engineering structures—Overview, limits and new ideas. *Mater. Struct.* 38, 578–592.
- Kim, H.-I., Han, M.-W., Song, S.-H., Ahn, S.-H., 2016. Soft morphing hand driven by SMA tendon wire. *Composites Part B: Engineering* 105, 138–148.
- Matia, Y., Gat, A.D., 2015. Dynamics of elastic beams with embedded fluid-filled parallel-channel networks. *Soft Robotics* 2, 42–47.
- Mendelson, N.H., 1978. Helical *Bacillus subtilis* macrofibers: morphogenesis of a bacterial multicellular macroorganism. *Proc. Natl. Acad. Sci.* 75, 2478–2482.
- Mosadegh, B., Polygerinos, P., Keplinger, C., Wennstedt, S., Shepherd, R.F., Gupta, U., Shim, J., Bertoldi, K., Walsh, C.J., Whitesides, G.M., 2014. Pneumatic networks for soft robotics that actuate rapidly. *Adv. Funct. Mater.* 24, 2163–2170.

- Polygerinos, P., Wang, Z., Overvelde, J.T., Galloway, K.C., Wood, R.J., Bertoldi, K., Walsh, C.J., 2015. Modeling of soft fiber-reinforced bending actuators. *IEEE Trans. Rob.* 31, 778–789.
- Reddy, J.N., 2013. *An Introduction to Continuum Mechanics*. Cambridge university press.
- Reddy, J.N., 2017. *Energy Principles and Variational Methods in Applied Mechanics*. John Wiley & Sons.
- Shepherd, R.F., Ilievski, F., Choi, W., Morin, S.A., Stokes, A.A., Mazzeo, A.D., Chen, X., Wang, M., Whitesides, G.M., 2011. Multigait soft robot. *Proc. Natl. Acad. Sci.* 108, 20400–20403.
- Sofla, A., Meguid, S., Tan, K., Yeo, W., 2010. Shape morphing of aircraft wing: status and challenges. *Mater. Des.* 31, 1284–1292.
- Suzumori, K., Endo, S., Kanda, T., Kato, N., Suzuki, H., 2007. A bending pneumatic rubber actuator realizing soft-bodied manta swimming robot. In: *Proceedings 2007 IEEE International Conference on Robotics and Automation*. IEEE, pp. 4975–4980.
- Takashima, K., Sugitani, K., Morimoto, N., Sakaguchi, S., Noritsugu, T., Mukai, T., 2014. Pneumatic artificial rubber muscle using shape-memory polymer sheet with embedded electrical heating wire. *Smart Mater. Struct.* 23, 125005.
- Tobushi, H., Hayashi, S., Hoshio, K., Makino, Y., Miwa, N., 2006. Bending actuation characteristics of shape memory composite with SMA and SMP. *J. Intell. Mater. Syst. Struct.* 17, 1075–1081.
- Wang, B., McDaid, A., Biglari-Abhari, M., Giffney, T., Aw, K., 2017. A bimorph pneumatic bending actuator by control of fiber braiding angle. *Sensors Actuators A: Physical* 257, 173–184.
- Wang, D., Li, L., Serjouei, A., Dong, L., Weeger, O., Gu, G., Ge, Q., 2018a. Controllable helical deformations on printed anisotropic composite soft actuators. *Appl. Phys. Lett.* 112, 181905.
- Wang, F., Yuan, C., Wang, D., Rosen, D.W., Ge, Q., 2020. A phase evolution based constitutive model for shape memory polymer and its application in 4D printing. *Smart Materials and Structures*.
- Wang, L., Yang, Y., Chen, Y., Majidi, C., Iida, F., Askounis, E., Pei, Q., 2018b. Controllable and reversible tuning of material rigidity for robot applications. *Mater. Today* 21, 563–576.
- Wang, T., Ge, L., Gu, G., 2018c. Programmable design of soft pneu-net actuators with oblique chambers can generate coupled bending and twisting motions. *Sens. Actuators A* 271, 131–138.
- Wang, T., Zhang, Y., Chen, Z., Zhu, S., 2019. Parameter Identification and Model-Based Nonlinear Robust Control of Fluidic Soft Bending Actuators. *IEEE/ASME Trans. Mechatron.* 24, 1346–1355.
- Westbrook, K.K., Kao, P.H., Castro, F., Ding, Y., Qi, H.J., 2011. A 3D finite deformation constitutive model for amorphous shape memory polymers: a multi-branch modeling approach for nonequilibrium relaxation processes. *Mech. Mater.* 43, 853–869.
- Yang, C., Boorugu, M., Dopp, A., Ren, J., Martin, R., Han, D., Choi, W., Lee, H., 2019. 4D printing reconfigurable, deployable and mechanically tunable metamaterials. *Mat. Horizons*.
- Yu, K., Ge, Q., Qi, H.J., 2014a. Reduced time as a unified parameter determining fixity and free recovery of shape memory polymers. *Nat. Commun.* 5, 3066.
- Yu, K., McClung, A.J., Tandon, G.P., Baur, J.W., Qi, H.J., 2014b. A thermomechanical constitutive model for an epoxy based shape memory polymer and its parameter identifications. *Mechanics of Time-Dependent Mat.* 18, 453–474.
- Zhang, Y.F., Zhang, N., Hingorani, H., Ding, N., Wang, D., Yuan, C., Zhang, B., Gu, G., Ge, Q., 2019. Fast-response, stiffness-tunable soft actuator by hybrid multimate-rial 3D printing. *Adv. Funct. Mater.* 29, 1806698.
- Zhao, Q., Wang, J., Cui, H., Chen, H., Wang, Y., Du, X., 2018. Programmed shape-morphing scaffolds enabling facile 3D endothelialization. *Adv Funct Mater* 28, 1801027.